Exact Inversion of the Exponential X-ray Transform for RSH SPECT

J.-M. Wagner[1], F. Noo[2], R. Clackdoyle[2]

[1]University of Liège, Montefiore Institute, 4000 Liège, Belgium (e-mail: JM.Wagner@ulg.ac.be)
[2]Medical Imaging Research Laboratory, University of Utah, Salt Lake City, UT 84108, USA (e-mail: noo@doug.med.utah.edu, rolf@doug.med.utah.edu)

Abstract

The RSH SPECT scanner provides parallel-beam attenuated projections for a fully 3D acquisition geometry. The geometry can be represented by circles on the unit sphere of projection directions, one circle for each position of the detector head. Unlike most other fully 3D geometries this one is particularly challenging because there are no 2D subsets in the data. When no attenuation is present, it is well-known that an unmeasured projection can be synthesized if it lies inside one of the measured circles. The main result of this work is that under some assumptions on the attenuation distribution, *attenuated* projections within a circle can be synthesized from available attenuated projections. One consequence is that RSH SPECT projections can be rebinned into a conventional SPECT geometry for which analytic attenuation correction techniques are available.

1 Introduction

In Single Photon Emission Computed Tomography (SPECT) imaging the objective is to establish the concentration of a radioactive tracer within the 3D body under investigation. The limitations in SPECT are mainly due to attenuation of the photons and to the poor sensitivity of the collimator-detector system. To overcome this latter limitation, a number of researchers have been considering alternatives to the conventional parallel-hole collimator (figure 1a).

The use of a rotating slant-hole (RSH) collimator with two (figure 1b) or four segments increases the detection sensitivity by allowing a higher photon count during the same acquisition period (Clack *et al* 1996). The collimator-detector system is successively placed at different angular positions around the body to be studied. For each of these positions, the collimator is rotated about its center, while allowing several projections (two or four according to the collimator used) to be acquired simultaneously. This acquisition mode constitutes the RSH SPECT geometry as described in Clack *et al* (1996).

The RSH SPECT scanner provides a set of attenuated projections. The exponential X-ray transform is a mathematical tool used in SPECT reconstruction for modeling and correcting for attenuation. Using the exponential X-ray transform, it is possible to reconstruct

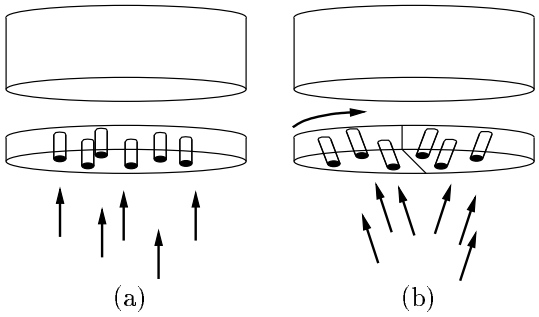

Figure 1: Different types of collimators. a) conventional parallel-hole collimator, b) RSH collimator.

the emission map with attenuation correction, assuming the attenuation is constant in the emission region. Attenuated projections can be converted to exponential parallel-beam (EPB) projections using a well-known point-by-point scaling (Markoe 1984). Moreover, even if the attenuation map is unknown, the consistency conditions of the exponential X-ray transform provide an effective method to find the scaling coefficients (Mennessier *et al* 1999).

In two-dimensions (2D), image reconstruction from EPB projections has been thoroughly studied over the past twenty-five years and is now well understood, especially due to the works of Tretiak and Metz (1980) and Metz and Pan (1995) for a constant attenuation over 2π. When the attenuation coefficient of the projections varies continuously from 0 to 2π, Kuchment and Schneiberg (1994) have derived a filtered back-projection (FBP) reconstruction algorithm. However, all these methods deal with data acquired on a full 2π range. Very recent works (Noo and Wagner 2001, Wagner 2002) provide an inversion formula for the case of only 180-degrees of exponential data. These results deal with EPB projections on 180-degrees whose attenuation coefficient is constant or can vary discontinuously from one projection to one another.

The acquisition geometry for RSH SPECT is a fully 3D geometry for which an inversion formula for the exponential X-ray transform has not yet been established. Only a few specific 3D geometries have been treated. In Weng *et al* (1996) and in Hazou and Solmon (1988), the EPB projections must be finely sampled on the unit sphere while the algorithm described in Wagner and Noo (2001) only handles collections of projections whose directions can be described as a union of great circles on the unit sphere. We observe that all these geometries assume measuring opposing views. Recently, Noo *et al* (2002a) have proposed some results for non-symmetric data sets. These results deal with EPB projections acquired on a half equatorial band on the unit sphere. Symmetric or not, we note that all these geometries satisfy Orlov's condition (Orlov 1975). Partial results have also been obtained for *any* geometry satisfying Orlov's condition (Noo *et al* 2002b).

We give a description of the general RSH geometry in section 2. In section 3, we generalize Orlov's result (Orlov 1975) and establish an exact rebinning algorithm that allows us to calculate new EPB projections (with any attenuation coefficient) from EPB projections given on a circle in the RSH geometry. In section 4, we use these new theoretical results to obtain a method of exact reconstruction from a set of complete EPB projections (complete in the sense of Orlov (1975)) for the RSH SPECT geometry. Finally, in section 5, we illustrate the efficacy of the methods of sections 3 and 4 using simulated data for a simple

geometry example.

2 The RSH SPECT geometry

Figure 2 illustrates the RSH SPECT geometry. In this figure, O is the origin of the unit sphere S^2. The orientation of the detector with respect to the origin is given by its unit normal vector $\underline{c}_i$. We assume N different positions of the detector ($i = 1, 2, \ldots, N$). Also, we assume that for each position i of the detector, the collimator has a slant angle equal to α_i. The unit vector $\underline{n}$ defines the direction of photon propagation through the collimator. When the collimator rotates 360 degrees about itself, the vector $\underline{n}$ describes, on the unit sphere, a circle C_i of angular aperture $2\alpha_i$ and whose axis of symmetry is the vector $\underline{c}_i$. The RSH SPECT geometry is mathematically defined by the trajectory Ω on the unit sphere corresponding to the union of all the circles C_i.

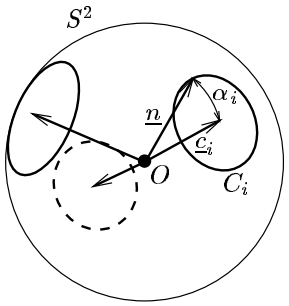

Figure 2: Illustration of the RSH SPECT geometry.

In a partially simplified model, the projection measured in the direction $\underline{n} \in \Omega$ can be described by the formula

$$g(\underline{n}, \underline{s}) = \int_{-\infty}^{+\infty} f(\underline{s} + t\underline{n}) \exp\Big(- \int_{t}^{+\infty} dl\, \mu_0(\underline{s} + l\underline{n})\Big)\,, \qquad \underline{s}.\underline{n} = 0\,, \tag{1}$$

where $f(\underline{x})$ is the concentration of the radioactive tracer to be reconstructed and $\mu_0(\underline{x})$ is a known function describing the attenuation of the medium. In this expression, vector $\underline{s}$ is orthogonal to $\underline{n}$ and is used to specify different lines of integration in the direction $\underline{n}$. In practice, $\underline{s}$ is defined by the detector locations for the $g(\underline{n}, \cdot)$ projection.

A simplification of the above relation between the data and the image f occurs when the activity is contained in a convex region where μ_0 is constant. We will assume that this condition holds. In this case, the reconstruction of f from g is equivalent to the reconstruction of f from the EPB projections

$$p_\mu(\underline{n}, \underline{s}) = \int_{-\infty}^{+\infty} f(\underline{s} + t\underline{n})\, e^{\mu t}\, dt, \qquad \underline{s}.\underline{n} = 0\,, \qquad \underline{n} \in \Omega \tag{2}$$

where μ is the (constant) value of μ_0 in the activity region. As explained in Markoe (1984), the EPB projection $p_\mu(\underline{n}, \underline{s})$ is obtained from $g(\underline{n}, \underline{s})$ by simple multiplication with a function $m_{\mu_0}(\underline{n}, \underline{s})$ calculated from the attenuation function $\mu_0(\underline{x})$. For example, if the convex region of constant attenuation including all the activity is a sphere centered at $\underline{x} = 0$,

$$g(\underline{n}, \underline{s}) = p_\mu(\underline{n}, \underline{s})\, m_{\mu_0}(\underline{n}, \underline{s}) \tag{3}$$

with

$$m_{\mu_0}(\underline{n},\underline{s}) = \exp\Big(\int_0^{+\infty} dl\, \mu_0(\underline{s}+l\underline{n})\Big)\,. \tag{4}$$

See Markoe (1984) for more general expressions of $m_{\mu_0}(\underline{n},\underline{s})$.

Note that, even if the attenuation map is not known, $g(\underline{n},\underline{s})$ can be converted into $p_\mu(\underline{n},\underline{s})$ in a reasonably accurate way using the consistency conditions for the exponential x-ray transform (Mennessier *et al* 1999).

3 Rebinning theory

Orlov (1975) pointed out that (in the absence of any attenuation) parallel-beam (PB) projections measured on a curve of the unit sphere can be used to synthesized unmeasured PB projections, whether or not the measured data provide enough information for exact reconstruction of f. For example, PB projections measured on one of the RSH circle C_i shown in figure 2 can be used to compute the PB projection of f in any direction $\underline{\alpha} \in C_i$.

In this section, we generalize the above result by Orlov; we show that EPB projections measured on a RSH circle C_i can be used to synthesize the EPB projection of f in any direction $\underline{\alpha} \in C_i$ for any finite attenuation coefficient μ_1. The synthesization or *rebinning* formula is conceptually valid for any closed curve on the unit sphere (Wagner 2002). However, for clarity and conciseness purposes the exposition is restricted to the case of a RSH circle.

3.1 Description of the rebinning formula

Let us consider one of the circles C_i making up Ω and let $\underline{\alpha}$ be a unit vector situated in the region of S^2 bounded by C_i. Figure 3 illustrates the situation. We use $\mathcal{C}(\underline{\alpha})$ to denote the great circle orthogonal to $\underline{\alpha}$ and we introduce four unit vectors $\underline{a}$, $\underline{b}$, $\underline{\theta}$ and $\underline{\theta}^\perp$ all lying on the great circle $\mathcal{C}(\underline{\alpha})$. The vectors $\underline{a}$ and $\underline{b}$ are defined mathematically by

$$\underline{a} = \frac{\underline{c}_i \times \underline{\alpha}}{||\underline{c}_i \times \underline{\alpha}||}, \quad \underline{b} = \underline{a} \times \underline{\alpha} \tag{5}$$

while

$$\begin{cases} \underline{\theta} &= \cos\theta\, \underline{a} + \sin\theta\, \underline{b} \\ \underline{\theta}^\perp &= -\sin\theta\, \underline{a} + \cos\theta\, \underline{b} \end{cases} \tag{6}$$

where θ belongs to the interval $[0, 2\pi]$. For the case where the vector $\underline{\alpha}$ corresponds to $\underline{c}_i$ we choose $\underline{a}$ arbitrarily on $\mathcal{C}(\underline{\alpha})$.

The great circle orthogonal to $\underline{\theta}$, denoted $\mathcal{C}(\underline{\theta})$, cuts the circle C_i at a point $\underline{n}$ given by

$$\underline{n} = \cos\psi(\theta)\, \underline{\alpha} + \sin\psi(\theta)\, \underline{\theta}^\perp \tag{7}$$

where the range of $\psi(\theta)$ depends on $\underline{\alpha}$ and is always a subset of $[0, 2\alpha_i]$. We show in section 3.2 that the function $\psi(\theta)$ is given by

$$\tan\frac{\psi(\theta)}{2} = \frac{-\sin(k\alpha_i)\, \cos\theta + \sqrt{\sin^2\alpha_i - \sin^2(k\alpha_i)\, \sin^2\theta}}{\cos\alpha_i + \cos(k\alpha_i)} \tag{8}$$

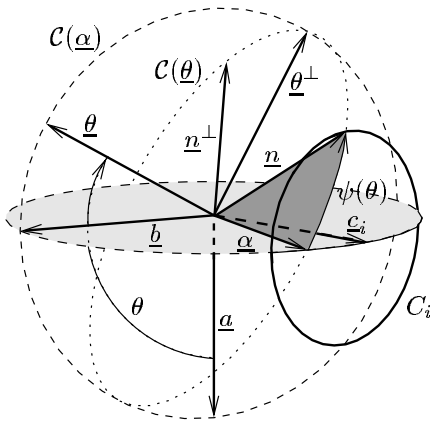

Figure 3: Rebinning from a set of exponential projections corresponding to a circle C_i.

where $(k\alpha_i)$ is the angle between $\underline{c}_i$ and $\underline{\alpha}$ ($k \in]0,1[$). Finally, we introduce the vector $\underline{n}^{\perp} = \underline{\theta} \times \underline{n} = -\sin\psi(\theta)\,\underline{\alpha} + \cos\psi(\theta)\,\underline{\theta}^{\perp}$.

From EPB projections $p_{\mu}(\underline{n},\underline{s})$ known for $\underline{n} \in C_i$, it is possible to calculate the EPB projection $p_{\mu_1}(\underline{\alpha},\underline{s})$ for any finite value μ_1 of the attenuation coefficient. To this end, the angular dependent exponential Radon transform (AD-ERT) of a 2D function is used. Appendix 1 gives an overview of this transform and its inverse, following the results by Kuchment and Shneiberg (1994).

Let $g(\theta,l)$ be the AD-ERT of the projection $p_{\mu_1}(\underline{\alpha},\underline{s})$,

$$g(\theta,l) = \int_{-\infty}^{+\infty} p_{\mu_1}(\underline{\alpha}, l\underline{\theta} + s\underline{\theta}^{\perp}) e^{\mu_2(\theta)s} ds\,, \tag{9}$$

with attenuation coefficient

$$\mu_2(\theta) = \frac{\mu - \mu_1\,\cos\psi(\theta)}{\sin\psi(\theta)}\,. \tag{10}$$

In section 2.3, we show that

$$g(\theta,l) = \int_{-\infty}^{+\infty} p_{\mu}(\underline{n}, l\underline{\theta} + t\underline{n}^{\perp}) e^{\mu_d(\theta)t} dt \tag{11}$$

with

$$\mu_d(\theta) = \frac{\mu\,\cos\psi(\theta) - \mu_1}{\sin\psi(\theta)} \tag{12}$$

for all $(\theta,l) \in [0,2\pi[\,\times\,]-\infty,+\infty[$. The expression on the right hand side of (11) is a sample of the 2D ERT of the RSH projection $p_{\mu}(\underline{n},\underline{s})$ with attenuation coefficient $\mu_d(\theta)$. A sample of the AD-ERT of the projection $p_{\mu_1}(\underline{\alpha},\underline{s})$ is therefore obtained by judiciously integrating in the plane of one of the available projections. By applying the relation (11) for all (θ,l), we obtain the complete AD-ERT of the projection $p_{\mu_1}(\underline{\alpha},\underline{s})$, from which $p_{\mu_1}(\underline{\alpha},\underline{s})$ is then obtained using the reconstruction formula of Kuchment and Shneiberg (1994):

$$p_{\mu_1}(\underline{\alpha},\underline{s}) = \int_0^{2\pi} g_F(\theta, \underline{s}.\underline{\theta})\, e^{-\mu_2(\theta)\underline{s}.\underline{\theta}^{\perp}}\, d\theta \tag{13}$$

where

$$g_F(\theta,l) = \int_{-\infty}^{+\infty} dl'\, h(\theta, l-l')\, g(\theta,l')\,, \tag{14}$$

with the filter $h(\theta,l)$ given by its Fourier transform

$$H(\theta,\sigma)=\int_{-\infty}^{+\infty}h(\theta,l)e^{-j2\pi l\sigma}d\sigma=\begin{cases}|\sigma|+j\,\mathrm{sgn}(\sigma)\,\mu_2'(\theta) & \text{if } |\sigma|>|\mu_2(\theta)|/(2\pi)\\ 0 & \text{otherwise}\end{cases}\tag{15}$$

In this expression, $\mu_2'(\theta)$ is the derivative of $\mu_2(\theta)$ and $j=\sqrt{-1}$.

In broad terms, the desired projection p_{μ_1} is obtained by filtered backprojection of its AD-ERT sinogram g. This sinogram is built row-by-row from ERT sinograms of existing projections.

In practice, large values of $\mu_2(\theta)$ can introduce numerical difficulties due to the form of $H(\theta,\sigma)$. Although any value of μ_1 can be used in principle, the safest choice is $\mu_1=\mu$ because $\mu_2(\theta)$ is then bounded by $\mu\tan\alpha_i$.

3.2 Derivation of the rebinning formula

In order to prove the rebinning formula of equations (9) to (12), we let

$$r(\theta,l)=\int_{-\infty}^{+\infty}p_\mu(\underline{n},l\underline{\theta}+t'\underline{n}^\perp)\,e^{\mu_d(\theta)t'}\,dt'\tag{16}$$

with $\mu_d(\theta)$ given by equation (12) and show that $r(\theta,l)$ is identical to $g(\theta,l)$ of equations (9) and (10).

From equation (2), we can write

$$p_\mu(\underline{n},l\underline{\theta}+t'\underline{n}^\perp)=\int_{-\infty}^{+\infty}f(l\underline{\theta}+t'\underline{n}^\perp+t\underline{n})\,e^{\mu t}\,dt\tag{17}$$

Introducing (17) into (16) gives

$$r(\theta,l)=\int_{-\infty}^{+\infty}\int_{-\infty}^{+\infty}f(l\underline{\theta}+t'\underline{n}^\perp+t\underline{n})\,e^{\mu t+\mu_d(\theta)t'}\,dt\,dt'\tag{18}$$

Anticipating the change of variables $t'\underline{n}^\perp+t\underline{n}=s'\underline{\alpha}+s\underline{\theta}^\perp$, we note from the definition of $\underline{n}$ and $\underline{n}^\perp$ that $t=s'\cos\psi(\theta)+s\sin\psi(\theta)$ and $t'=-s'\sin\psi(\theta)+s\cos\psi(\theta)$. Using these expressions for t and t', and expression (12) for $\mu_d(\theta)$ we see that

$$\begin{aligned}\mu t+\mu_d(\theta)t' &= \mu\,[s'\cos\psi(\theta)+s\sin\psi(\theta)]\\ &\quad+\frac{\mu\cos\psi(\theta)-\mu_1}{\sin\psi(\theta)}\,[-s'\sin\psi(\theta)+s\cos\psi(\theta)]\\ &= \mu_1 s'+\frac{\mu-\mu_1\cos\psi(\theta)}{\sin\psi(\theta)}s\\ &= \mu_1 s'+\mu_2(\theta)s\end{aligned}\tag{19}$$

where $\mu_2(\theta)$ is given by (10). Similar manipulations show that $\mu\underline{n}+\mu_d(\theta)\underline{n}^\perp=\mu_1\underline{\alpha}+\mu_2(\theta)\underline{\theta}^\perp$ which has the geometrical interpretation illustrated in figure 4. Performing the change of variables from (t,t') to (s,s') in (18) and using (19) gives

$$r(\theta,l)=\int_{-\infty}^{+\infty}\int_{-\infty}^{+\infty}f(l\underline{\theta}+s'\underline{\alpha}+s\underline{\theta}^\perp)\,e^{\mu_1 s'+\mu_2(\theta)s}\,ds\,ds'\tag{20}$$

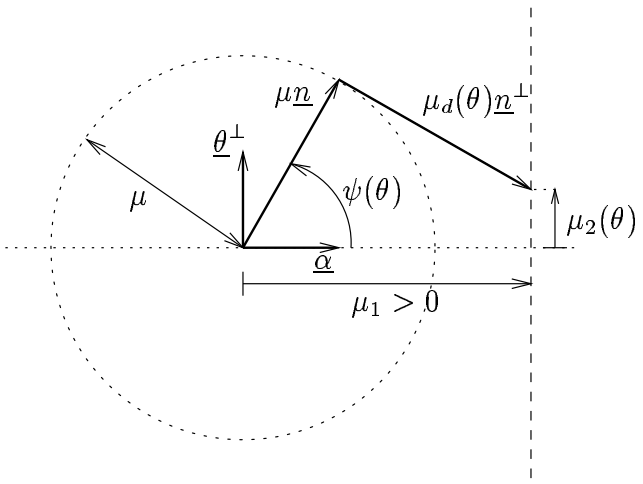

Figure 4: Geometrical description of the relationship between $\mu_d(\theta)$ and $\mu_2(\theta)$.

At last, we rearrange terms and use equation (2) to obtain

$$\begin{aligned} r(\theta,l) &= \int_{-\infty}^{+\infty}\left\{\int_{-\infty}^{+\infty} f(s'\underline{\alpha}+l\underline{\theta}+s\underline{\theta}^{\perp})\,e^{\mu_1 s'}\right\} e^{\mu_2(\theta)s}\,ds \\ &= \int_{-\infty}^{+\infty} p_{\mu_1}(\underline{\alpha},l\underline{\theta}+s\underline{\theta}^{\perp})\,e^{\mu_2(\theta)s}\,ds \end{aligned} \tag{21}$$

This last expression is identical to $g(\theta,l)$, the 2D AD-ERT of $p_{\mu_1}(\underline{\alpha},\underline{s})$, as given by equation (9).

To derive expression (8) for $\psi(\theta)$, we use the fact that $\underline{n}=\cos\psi(\theta)\,\underline{\alpha}+\sin\psi(\theta)\,\underline{\theta}^{\perp}$ is lying on the circle C_i :

$$\underline{n}.\underline{c}_i = \cos\alpha_i \tag{22}$$

Using $\underline{c}_i=\cos(k\alpha_i)\,\underline{\alpha}-\sin(k\alpha_i)\,\underline{b}$ and replacing $\underline{n}$ by its expression in equation (22) gives the following trigonometric equation w.r.t $\psi(\theta)$:

$$\cos\psi(\theta)\,\cos(k\alpha_i)-\sin\psi(\theta)\,\sin(k\alpha_i)\,\cos\theta=\cos\alpha_i \tag{23}$$

To solve this equation, we let $x=\tan(\psi(\theta)/2)$. Expressing $\cos\psi(\theta)$ and $\sin\psi(\theta)$ in terms of x in equation (23) gives an equation of the second order w.r.t x. The resolution of this last equation gives expression (8) for $\tan(\psi(\theta)/2)$, which corresponds to the solution for which $\psi(\theta)$ lies in $[0,2\alpha_i]$.

4 RSH-SPECT reconstruction

From the new theoretical results of section 3, we have derived a data completeness condition for inversion of the exponential X-ray transform in RSH-SPECT geometry (Wagner 2002) :

> *For any set Ω of circles on the unit sphere whose centers $\underline{c}_i(i=1,...,N)$ lie on a common great circle $\mathcal{C}(\underline{e}_z)$, the activity f can be accurately reconstructed from the corresponding exponential parallel-beam projections if every great circle of the unit sphere intersects Ω.*

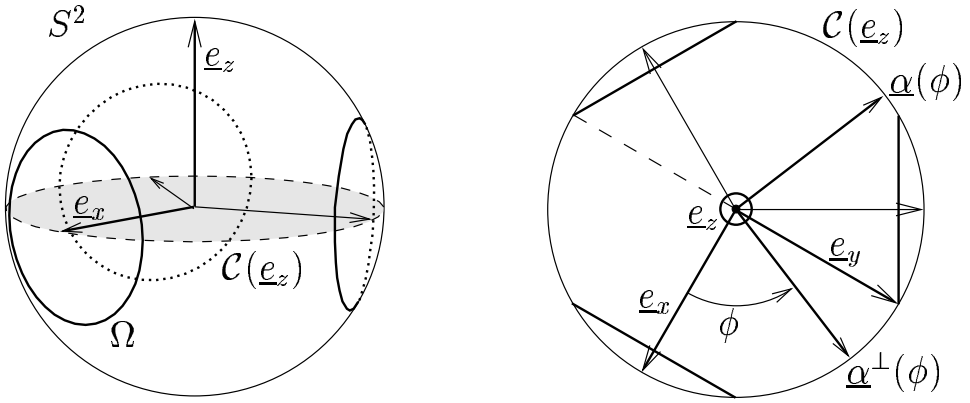

Figure 5: (left) Example of an RSH-SPECT geometry without opposing views. (right) left figure viewed from the top with illustration of the direction $\underline{\alpha}(\phi)$ of synthesized projections.

This condition is equivalent to Orlov's condition (Orlov 1975) for the inversion of the X-ray transform in the non-attenuated case. This result is particularly interesting because it shows that opposing views are not required for exact and stable reconstruction.

One example of RSH-SPECT geometry which satisfies our condition is given in figure 5a. It consists of 3 circles of angular aperture equal to 60 degrees and whose centers are separated by 120 degrees.

The validity of the data completeness condition is proved as follows. Consider a set of data Ω which satisfies this condition. From the EPB projections $p_\mu(\underline{n}, \underline{s})$ known on Ω, the rebinning technique can be used to (1) synthesize the EPB projection $p_\mu(\underline{\alpha}, \underline{s})$ for any direction $\underline{\alpha}$ that lies on the great circle $\mathcal{C}(\underline{e}_z)$ and is inside one of the RSH circles, and (2) synthesize the EPB projection $p_{-\mu}(\underline{\alpha}, \underline{s})$ for any direction $\underline{\alpha}$ that lies on the great circle $\mathcal{C}(\underline{e}_z)$ and is not inside one of the RSH circles, since $p_{-\mu}(\underline{\alpha}, \underline{s}) = p_\mu(-\underline{\alpha}, \underline{s})$ and $-\underline{\alpha}$ is inside one of the RSH circles when $\underline{\alpha}$ is not. Let $\underline{\alpha}(\phi) = (\cos\phi, \sin\phi, 0)$ describes one half of $\mathcal{C}(\underline{e}_z)$ with $\phi \in [0, \pi[$, as illustrated in figure 5. From the synthesized projections, it is always possible to create a set of projections $p_{\mu_1}(\underline{\alpha}(\phi), \underline{s})$ with a function $\mu_1(\phi)$ that is piecewise constant, has a finite number of discontinuities, and is such that $|\mu_1(\phi)| = \mu$. Figure 6 illustrates such a function for the RSH-SPECT geometry of figure 5. From the projections $p_{\mu_1}(\underline{\alpha}(\phi), \underline{s})$ obtained for $\phi \in [0, \pi[$, f can be reconstructed slice-by-slice perpendicular to $\underline{e}_z$ using the 2D reconstruction formula given in Wagner (2002) and also in Pan *et al* (2002). This 2D formula, given in appendix 2, inverts the AD-ERT over 180 degrees for an attenuation coefficient of the form of $\mu_1(\phi)$.

5 Simulations and Results

In this section, we study an example RSH SPECT geometry. The set Ω under consideration consists of 3 circles whose centers $\underline{c}_i$ are situated on the great circle $\mathcal{C}(\underline{e}_z)$ at regular intervals of 60 degrees and with a slant angle of 30 degrees (for $i = 1, 2, 3$). Figure 6 illustrates the situation. According to Orlov (1975), this set is complete because all great circles on the unit sphere intersect Ω. An exact reconstruction is therefore possible in the non-attenuated case. We show below that exact reconstruction is also possible for the attenuated case.

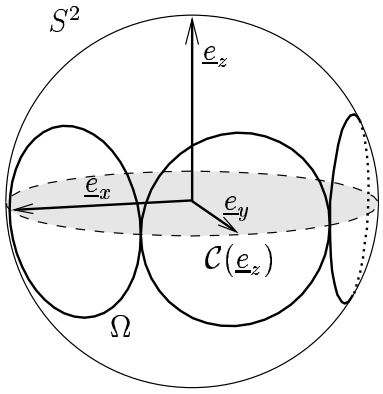

Figure 6: Illustration of the RSH SPECT geometry used for the experiment of section 4.

There are 3 distinct positions of the detector and we have simulated attenuated projections for 32 angular positions of the collimator rotating about its own axis, which makes a total of $3 \times 32 = 96$ simulated attenuated projections for this RSH SPECT geometry. Each attenuated projection was sampled on a grid of 100^2 pixels of side 1.5 mm. Each data point in a given attenuated projection was computed using analytical formulas based on (1). The emission map was a simplified model of the heart consisting of three ellipsoids, two of which modeled the ventricles with 20% of the specific activity of the myocardium. The attenuation map consisted of 4 ellipsoids, representing the thorax, the two lungs, and the spinal column. Figure 7 shows the emission and attenuation maps for two slices in different orientations.

As can be seen in figure 7, the attenuation is constant in the emission region. For reconstruction of f, we converted the simulated attenuated projections into EPB projections using the method of Markoe (1984) with the known expression of the attenuation map. The attenuation coefficient for the resulting EPB projections was $\mu = 0.15/\text{cm}$. We then applied the rebinning method (equations (9) to (15)) with $\mu_1 = \mu$ to synthesize the EPB projections $p_\mu(\underline{\alpha}, \underline{s})$ for 181 directions $\underline{\alpha}$ uniformly sampled on half of the great circle $\mathcal{C}(\underline{e}_z)$ with an angular step of 1 degree. The synthesized projections were obtained on a grid of 100^2 pixels of side 1.5 mm. Figure 8 shows one of the 181 EPB projections synthesized by the rebinning method.

The 181 synthesized EPB projections constitute a set of projections in the conventional (180-degree) parallel-hole collimator SPECT geometry. For this configuration an exact inversion formula now exists (Noo and Wagner 2001). We applied this algorithm to reconstruct, slice by slice perpendicular to $\underline{e}_z$, the image f on a grid of 100^3 voxels of side 1.5 mm. The quality of the reconstruction given in figure 9 illustrates the efficacy of the reconstruction method. More simulations and an example using real phantom data can be found in Wagner *et al* (2002).

6 Conclusions

We have derived an exact rebinning method that allows new exponential parallel-beam projections to be calculated from a set of known exponential parallel-beam projections given on a circle of the unit sphere of directions. These new theoretical results generalize

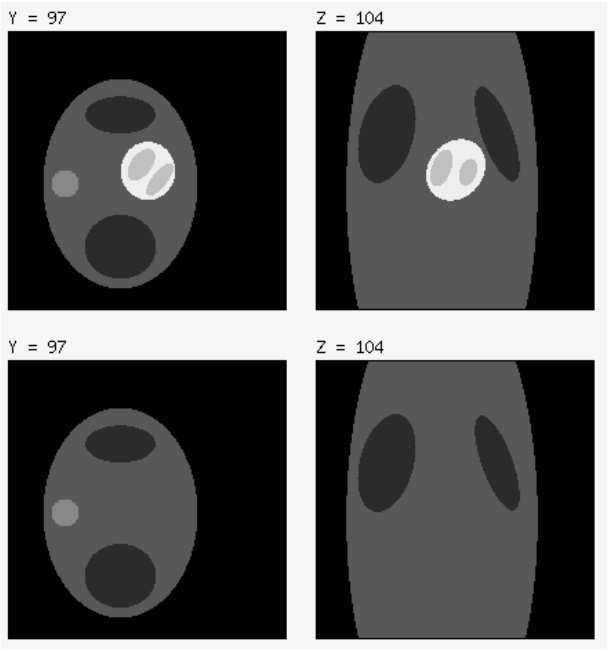

Figure 7: Illustration of the emission and attenuation maps. The images in the left column shows a tranverse slice while the images in the right column shows a coronal slice. The top row shows a superimposition of the attenuation and emission maps. The bottom row shows the attenuation map only. The emission map lies in a region of constant attenuation $\mu = 0.15\text{cm}^{-1}$.

Orlov's theory for the non-attenuated case. As a corollary, we have presented an exact method of inversion of the exponential X-ray transform for any RSH-SPECT geometry that satisfies Orlov's condition and whose detector positions $\underline{c}_i$ lie on a common great circle say $\mathcal{C}(\underline{e}_z)$ (i.e. the detector gantry axis is $\underline{e}_z$). Our results were tested using simulations which illustrated the exactness of the method.

Acknowledgments

This work was partially supported by the National Institutes of Health, grant number RO1 HL55610. Its contents are solely the responsibility of the authors and do not necessarily represent the official views of the National Institutes of Health.

This work was achieved for the most part while F. Noo was a Research Associate with the Belgian National Fund for Scientific Research.

The authors thanks Xiaochuan Pan for the preprint of his paper on π-schemes for the exponential Radon transform and the uniqueness of their inverses.

Appendix 1

In this section, we give a brief overview of the AD-ERT of a 2D function and its inverse, following the results by Kuchment and Shneiberg (1994). The 2D function is defined as

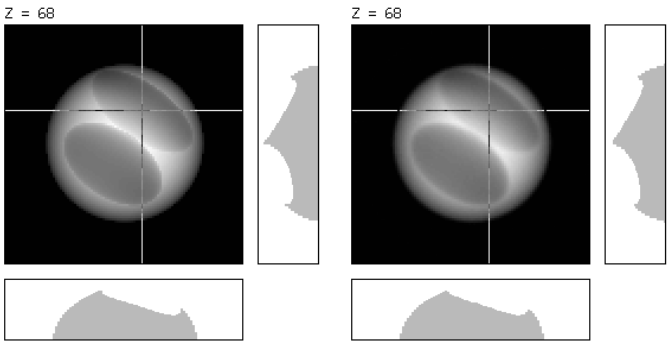

Figure 8: Illustration of the rebinning method ($k = 0.5$). Left: Ideal projection. Right: Synthesized projection.

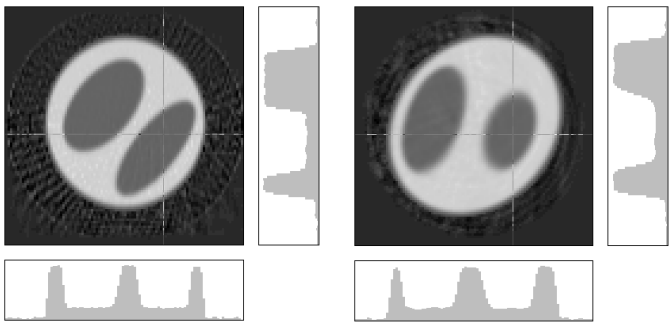

Figure 9: Reconstruction of the emission map of figure 7 from simulated RSH-SPECT data using the geometry of figure 6. Left: transverse slice. Right: coronal slice.

$p(\underline{s})$ with $\underline{s} = (u, v)$, using Cartesian coordinates u and v measured along some directions $\underline{a}$ and $\underline{b}$, respectively.

Let $\underline{\theta} = \cos\theta\,\underline{a} + \sin\theta\,\underline{b}$ and $\underline{\theta}^{\perp} = -\sin\theta\,\underline{a} + \cos\theta\,\underline{b}$, with $\theta \in [0, 2\pi[$. Let $l \in]-\infty, +\infty[$. Let $\mu(\theta)$ be a continuously differentiable function of period 2π. By definition, the AD-ERT of p is the function which associates

$$g(\theta, l) = \int_{-\infty}^{+\infty} w(l\,\underline{\theta} + s\,\underline{\theta}^{\perp})\, e^{\mu(\theta)}\, ds \tag{24}$$

to each value of (θ, l). For a fixed θ, the set of values of $g(\theta, l)$ obtained by varying l is an exponentially-attenuated projection of w.

A filtered backprojection reconstruction of p from g is possible when g is known for $(\theta, l) \in [0, 2\pi[\times]-\infty, +\infty[$. The filtering step of this reconstruction modifies the projections into

$$g_F(\theta, l) = \int_{-\infty}^{+\infty} h(\theta, l - l')\, g(\theta, l')\, dl' \tag{25}$$

where $h(\theta, l)$ is given by equation (15). The backprojection step gives

$$p(\underline{s}) = \int_0^{2\pi} g_F(\theta, l)\Big|_{l=\underline{s}\cdot\underline{\theta}}\, e^{-\mu(\theta)\,\underline{s}\cdot\underline{\theta}^{\perp}}\, d\theta \tag{26}$$

References

Clack R, Christian P E, Defrise M and Welch A E 1996 Image reconstruction for a novel SPECT system with rotating slant-hole collimators *Conference Record of the 1995 IEEE Nuclear Symposium and Medical Imaging Conference* 1948-1952

Hazou I A and Solmon D C 1988 Inversion of the exponential X-ray transform. I:Analysis *Math. Methods in the Applied Sciences* **10(10)** 561-574

Kuchment P and Shneiberg I 1994 Some Inversion formulas in the Single Photon Emission Computed Tomography *Appl. Anal.*, **53** 221-231

Markoe A 1984 Fourier inversion of the attenuated X-ray transform *SIAM J. Math. Anal.* **15(4)** 718-722

Mennessier C, Noo F, Clack R, Bal G and Desbat L 1999 Attenuation correction in SPECT using consistency conditions for the exponential ray transform *Phys. Med. Biol.* **44** 2483-2510

Metz C E and Pan X 1995 A unified analysis of exact methods of inverting the 2D exponential Radon tranform, with implications for Noise control in SPECT *IEEE Trans. Med. Imag.* **14(4)** 643-658

Noo F and Wagner J-M 2001 Image reconstruction in 2D SPECT with 180-degree acquisition *Inv. Prob.* **17** 1357-1371

Noo F, Clackdoyle R and Wagner J-M 2002a Inversion of the 3D exponential X-ray transform for a semi-equatorial band *Phys. Med. Biol. (this issue).*

Noo F, Clackdoyle R and Wagner J-M 2002b Data Sufficiency and an Inversion Formula for Fully Three-Dimensional Image Reconstruction from Exponential X-ray Projections *Conference Record of the 2001 IEEE Nuclear Symposium and Medical Imaging Conference, IEEE Catalog Number 0-7803-7324-3* abstract number M9C-4

Orlov S S 1975 Theory of three dimensional reconstruction. 1. Conditions of a complete set of projections *Sov. Phys.-Crystallogr* **20** 312-314

Pan X, Kao C-M and Metz C 2002 A family of π-scheme exponential Radon transform and the uniqueness of their inverses *Inverse Problems* (to appear)

Tretiak O and Metz C 1980 The exponential Radon transform *SIAM J. Appl. Math.* **39(2)** 341-354

Wagner J-M 2002 *Méthodes analytiques pour la correction d'atténuation en tomographie tridimensionnelle par émission monophotonique* PhD thesis: Collection des Publications de la Faculté des Sciences Appliquées (University of Liège, Belgium)

Wagner J-M and Noo F 2001 Three-dimensional image reconstruction from exponential parallel-beam projections *IEEE Trans. Nucl. Sci.* **48(3)** 743-749

Wagner J-M, Noo F, Clackdoyle R, Bal G and Christian P 2002 Attenuation Correction for Rotating Slant-Hole (RSH) SPECT using Exact Rebinning *Conference Record of the 2001 IEEE Nuclear Symposium and Medical Imaging Conference, IEEE Catalog Number 0-7803-7324-3* abstract number M8-5

Weng Y, Zeng G L and Gullberg G T 1996 Filtered backprojection algorithm for attenuated parallel and cone-beam projections sampled on a sphere *Three-dimensional Image Reconstruction In Radiation and Nuclear Medicine, eds. Grangeat P and Amans J-L (Dordrecht: Kluwer)* 19-34